Aerospace Systems
https://doi.org/10.1007/s42401-021-00089-8

ORIGINAL PAPER

End-of-life geostationary satellite removal using realistic flat solar sails

Hao Mei[1] · Christopher J. Damaren[1] · Xingqun Zhan[2]

Received: 24 September 2020 / Revised: 22 February 2021 / Accepted: 18 March 2021

Abstract

This paper proposes an analytical solution of removing end-of-life GEO satellites to the GEO graveyard region using realistic flat solar sails. Different from the ideal solar sail model, the proposed realistic flat solar sail model applies the realistic solar sail thrust model, and the sail cone angle is constrained within $[0^\circ, 85^\circ]$. The dynamic system of a GEO satellite equipped with a realistic flat solar sail is constructed based on the Gauss's variation of parameter (VOP) equations, and linearized along a nominal trajectory. Control angles of the sail are generated using the linear optimal tracking controller. Iterations of linearization are applied to gradually reduce the inaccuracy of the linearized systems, thus reducing the terminal state error. Simulations indicate that, end-of-life GEO satellites are successfully removed to the GEO graveyard region in 350 days using the proposed control approach. The negative impact of using realistic flat solar sails in the end-of-life GEO satellite removal mission is evident but not significant. Compared to using ideal solar sails, a small increase in the A/m of spacecraft from 0.14 to 0.16 $\mathrm{kg/m^2}$ is required.

Keywords GEO debris removal · Solar radiation pressure · Realistic solar sail

1 Introduction

The increasing population of space debris in the Geostationary Earth Orbit (GEO) has been alarming in recent years [1–3]. The latest annual reports ESA Annual Space Environment Report [4] and Classification of Geosynchronous Objects [5] published by the European Space Agency (ESA) indicate that, the number of all the known space debris in GEO has been increasing since 2001, and exceeded 1000 in 2018. At present, debris takes up more than 70% of the total object amount. The Galaxy 15 incident [6] also implies that, without further orbit control, nonfunctional satellites may drift because of luni-solar disturbances, allowing them to wander the GEO belt and threaten active satellites.

To mitigate the severe situation, the Inter-Agency Space Debris Coordination Committee (IADC) published Space Debris Mitigation Guidelines [7] in 2007. According to the guidelines, the GEO protected region (Table 1) should be protected in respect of space debris generation. End-of-life satellites in GEO should be removed far enough above GEO so as not to interfere with the GEO protected region. Studies [8,9] have found that fulfilling the two conditions in Table 2 (which also define the GEO graveyard region) at the end of disposal will ensure an orbit that remains above the GEO protected region.

There exists limited research on removing end-of-life GEO satellites to the GEO graveyard region using solar radiation pressure (SRP). In [10], the feasibility of re-orbiting three-axis stabilized GEO satellites to the GEO graveyard region using SRP was first demonstrated. Ref. [11] proposed the TugSat concept, in which a 1000 kg non-functional GEO satellite is removed to the GEO graveyard region using an 800 $\mathrm{m^2}$ solar sail. The removal is accomplished by first raising the orbit semi-major axis by 350 km, then reducing the eccentricity to zero. Ref. [12] derived an analytical removal solution based on Lyapunov control theory combined with the calculus of variations. In that work, a partical swarm optimizer (PSO) is used to optimize user designed parameters, which then generates the robust locally time optimal removal

✉ Hao Mei
hao.mei@mail.utoronto.ca

Christopher J. Damaren
damaren@utias.utoronto.ca

Xingqun Zhan
xqzhan@sjtu.edu.cn

1 University of Toronto Institute for Aerospace Studies, 4925 Dufferin Street, Toronto, ON M3H 5T6, Canada

2 Shanghai Jiaotong University School of Aeronautics and Astronautics, 800 Dongchuan Road, Shanghai 200240, China

Table 1 The GEO protected region

Property	Requirement
GEO	35786 km
Upper bound	GEO + 200 km
Lower bound	GEO − 200 km
Inclination	[−15°, +15°]

Table 2 The GEO graveyard region

Property	Requirement
Perigee altitude	A minimum increase of 235 km + (1000 · C_R · A/m) 235 km : the sum of the upper altitude of the GEO protected region (200 km) and the maximum descent due to luni-solar and geo-potential perturbations (35 km) C_R : the solar radiation pressure (SRP) coefficient A/m : the area to dry mass ratio
Eccentricity	[0, 0.003]

solutions. In [13], an analytical removal solution was proposed which requires a small area-to-mass (A/m) ratio of spacecraft. Although end-of-life GEO satellites are successfully removed to the GEO graveyard region using SRP and impulsive thrusts, there exists terminal state error between the terminal state and the desired state. Ref. [14] proposed a feedback pseudospectral (PS) method to reduce the terminal state error in [13]. In that work, the iterations of the open-loop PS method and the linear feedback controller are applied to search the global minimum of the cost function. The global minimum is reached at the price of a large computation cost.

In this work, we apply the "iterations of linearization" control approach to remove end-of-life GEO satellites to the GEO graveyard region. The proposed control approach significantly reduces the terminal state error in [13], as well as the computation cost caused by the numerical approach in [14]. In theory, the applied "iterations of linearization" control approach is only able to find a quasi-local optimal solution. A quasi-local optimal solution is acceptable for the end-of-life GEO satellite removal mission, since the GEO graveyard region is broad and the requirements on the orbital elements are not strict.

Among all the existing research on removing end-of-life GEO satellites to the GEO graveyard region using solar sails, the ideal solar sail model is applied. However, ideal solar sails are different from realistic ones, and the differences could have negative impacts on the end-of-life GEO satellite removal mission. For example, for realistic solar sails, the sail cone angle is constrained and can't reach 90° (SRP can't be turned off) due to the temperature and structure reasons. This results in a so-called "leeward force" [15], which always exits along the Sun-sail direction. The "leeward force" is unfavourable for the end-of-life GEO satellites removal mission, because the "leeward force" will decrease the orbit altitude when the satellites move toward the Sun.

Ref. [16] shows that there is a significant deviation in force magnitude between the realistic solar sail and the ideal solar sail model. Ref. [15] conducted thorough comparisons between the ideal and realistic solar sails. Different from ideal solar sails, there always exists a thrust component in the sail transverse direction for realistic solar sails. Realistic solar sails are not always flat, there could be small-scale (wrinkles and crinkles) and large-scale (billow and drop) irregularities in the sail surface. Because of temperature and structure reasons, the sail cone angle is constrained within [0°, 85°] for realistic solar sails. Ref. [17] compared the thrusts generated by the ideal solar sails and the realistic ones, concluding that the impacts of the sail surface properties and sail shape on the solar sail thrust are not significant.

In this work, we propose a realistic flat solar sail model. Based on the results in [15], the realistic solar sail thrust model is applied. The cone angle of the sail is constrained. Considering the results in [17], the sail deformation and sail surface irregularities are ignored. The proposed realistic flat solar sail model is detailed in Sect. 2.

The main contributions of this work are as follows. First we apply the "iterations of linearization" control approach to remove end-of-life GEO satellites to the GEO graveyard region using solar sailing. The proposed control approach significantly reduces the terminal state error in [13], as well as the computation cost in [14]. Second, a realistic flat solar sail model is proposed and utilized in the removal mission. The impacts of the removal using realistic flat solar sails are analyzed.

This paper is organized as follows. Section 2 presents the dynamic model and the system dynamics of a GEO satellite equipped with a realistic flat solar sail. Section 3 elaborates on the solar sail control approach, and it's utilized to remove end-of-life GEO satellites in Sect. 4. Section 5 draws conclusions.

2 Spacecraft dynamics and system modelling

2.1 SRP

For ideal solar sails, all the incoming photons are reflected. The acceleration due to SRP for ideal solar sails is given by [18, page 39]

$$\boldsymbol{f}_{\text{ideal}} = \left[2P_{\odot} \cdot (A/m) \cdot \cos^2\alpha\right]\boldsymbol{n}. \qquad (1)$$

SPI Journal: 42401 MS: 0089 TYPESET DISK LE CP Disp.:2021/6/6 Pages: 12 Layout: Large

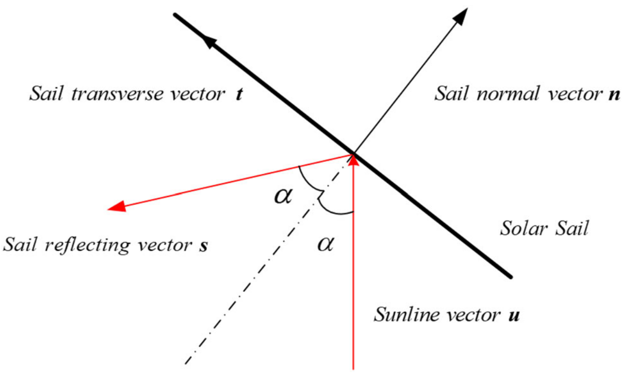

Fig. 1 2D solar sail model

Here $P_{\odot}$ denotes the magnitude of SRP which at 1 AU from the Sun is equal to 4.56×10^{-6} N/m^2. A/m is the area to mass ratio of spacecraft, and α denotes the cone angle (the pitch angle in the 2D case) of the solar sail, which is the angle between the sail normal vector $\boldsymbol{n}$ and the sun-line vector $\boldsymbol{u}$ (Fig. 1).

In this work. we propose a realistic flat solar sail model, which differs from an ideal one in two aspects.

1. Solar sail thrust
   After absorbing all the incoming photons, realistic solar sails only reflect part of (ratio $\tilde{r}$) the total photons, while the other part of photons (ratio $(1-\tilde{r})$) are re-emitted by thermal radiation. Among all the reflected photons, s ratio of photons are reflected in the $\boldsymbol{s}$ direction (Fig. 1), while $(1-s)$ ratio are reflected in non-specular directions. In this process, acceleration caused by SRP is composed by three parts, namely, the acceleration due to absorption $\boldsymbol{f}_a$, the acceleration due to reflection $\boldsymbol{f}_r$, and the acceleration due to re-radiation $\boldsymbol{f}_e$, and they are given by [18, page 48-49]

$$
\begin{aligned}
\boldsymbol{f}_a &= P_{\odot}\frac{A}{m}\left[(\cos^2\alpha)\boldsymbol{n} + (\cos\alpha\sin\alpha)\boldsymbol{t}\right],\\
\boldsymbol{f}_r &= P_{\odot}\frac{A}{m}\Big[\left(\tilde{r}s\cos^2\alpha + B_f(1-s)\tilde{r}\cos\alpha\right)\boldsymbol{n}\\
&\quad - (\tilde{r}s\cos\alpha\sin\alpha)\boldsymbol{t}\Big],\\
\boldsymbol{f}_e &= \left[P_{\odot}\frac{A}{m}(1-\tilde{r})\,\frac{\xi_f B_f - \xi_b B_b}{\xi_f + \xi_b}\cos\alpha\right]\boldsymbol{n}.
\end{aligned}
\tag{2}
$$

   Here B_f, B_b and ξ_f and ξ_b are the non-Lambertian coefficients and surface emissivity of the front and back side of the sail. $\boldsymbol{t}$ denotes the sail transverse vector (Fig. 1), and $\boldsymbol{t} = (\boldsymbol{u} - (\boldsymbol{u}\cdot\boldsymbol{n})\boldsymbol{n})/|\boldsymbol{u} - (\boldsymbol{u}\cdot\boldsymbol{n})\boldsymbol{n}|$.
   By adding the three components in Eq. (2) and recognizing accelerations in the sail normal and transverse directions, the accelerations due to SRP for realistic solar sails are

$$
\begin{aligned}
\boldsymbol{f}_n &= \Bigg(P_{\odot}\frac{A}{m}\Big[(1+\tilde{r}s)\cos^2\alpha + B_f(1-s)\tilde{r}\cos\alpha\\
&\quad + (1-\tilde{r})\,\frac{\xi_f B_f - \xi_b B_b}{\xi_f + \xi_b}\cos\alpha\Big]\Bigg)\boldsymbol{n},\\
\boldsymbol{f}_t &= \left(P_{\odot}\frac{A}{m}(1-\tilde{r}s)\cos\alpha\sin\alpha\right)\boldsymbol{t}.
\end{aligned}
\tag{3}
$$

   In this work, we apply the sail optical parameters (Table 3) [18, page 50] for a square/heliogyro solar sail derived from the NASA Jet Propulsion Laboratory (JPL) comet Halley rendezvous study.
2. Constraint in the cone angle
   For ideal solar sails, there is no constraint in the sail control angles. However, for realistic solar sails, to avoid the possible temperature and structure failure, the cone angle α is constrained within $[0°, 85°]$ [15]. This constraint is important and also unfavourable for the end-of-life GEO satellites removal mission, since the resulting "leeward force" always exits along the Sun-sail direction and will decrease the orbit altitude when the satellites move toward the Sun.

Table 3 Optical coefficients for an ideal/JPL square/JPL Heliogyro solar sail

	$\tilde{r}$	$\tilde{s}$	ξ_f	ξ_b	B_f	B_b
Ideal sail	1	1	0	0	2/3	2/3
Square sail	0.88	0.94	0.05	0.55	0.79	0.55
Heliogyro sail	0.88	0.94	0.05	0.55	0.79	0.55

In the applied realistic flat solar sail model, we assume that there is no sail deformation and surface irregularity during the removal process. The eclipse by the Earth is included in the dynamic model. A GEO satellite experiences eclipse by the Earth in the summer and winter. This work applies the cylindrical eclipse shadow model, which is detailed in [13].

2.2 Perturbative accelerations

This work utilizes the perturbative dynamic model proposed in [13], which is based on the magnitude comparisons of different accelerations exerted on GEO satellites, and the drifts of orbital elements due to each perturbative term over the removal period. The total acceleration exerted on a GEO satellite can be described as $\ddot{\boldsymbol{r}} = \ddot{\boldsymbol{r}}_{\oplus} + \ddot{\boldsymbol{r}}_3 + \ddot{\boldsymbol{r}}_{\boldsymbol{SRP}}$. Here, $\ddot{\boldsymbol{r}}_{\oplus}$ denotes the Earth gravitational acceleration, including the two-body acceleration and Earth gravitational perturbations, $\ddot{\boldsymbol{r}}_3$ is the third-body (the Sun and Moon) gravitational perturbation, and $\ddot{\boldsymbol{r}}_{\boldsymbol{SRP}}$ denotes the acceleration due to SRP.

SPI Journal: 42401 MS: 0089 ☐ TYPESET ☐ DISK ☐ LE ☐ CP Disp.:2021/6/6 Pages: 12 Layout: Large

Earth's gravitational potential is given by [19, page 545]

$$U=\frac{\mu_\oplus}{r}-\frac{\mu_\oplus}{r}\sum_{l=2}^{\infty}J_l\left(\frac{R_\oplus}{r}\right)^l P_l[\sin\phi]$$
$$+\frac{\mu_\oplus}{r}\sum_{l=2}^{\infty}\sum_{m=1}^{l}\left(\frac{R_\oplus}{r}\right)^l P_{l,m}[\sin\phi]$$
$$\times\left\{C_{l,m}\cos(m\lambda_{\text{sat}})+S_{l,m}\sin(m\lambda_{\text{sat}})\right\}. \tag{4}$$

Here, $\mu_\oplus$ is the Earth's gravitational parameter, r the magnitude of the satellite position vector in the Earth Centred Earth Fixed (ECEF) frame, ϕ and λ are the latitude and longitude of satellite, P_l ($P_{l,m}$) denotes the conventional (associated) Legendre polynomials, and J_l ($C_{l,m}$, $S_{l,m}$) are the zonal (sectoral and tesseral) harmonics. Earth's gravitational acceleration in the ECEF frame can be obtained by taking the gradient of the total gravitational potential. As in [13], our work uses the second and the third order terms of the Earth's gravitational perturbation in the dynamic model.

The equation of motion of a three-body system is given by [19, page 574]

$$\ddot{\boldsymbol{r}}_{\oplus\,\text{sat}}=-\frac{\mu_\oplus\boldsymbol{r}_{\oplus\,\text{sat}}}{r^3_{\oplus\,\text{sat}}}+\mu_3\left(\frac{\boldsymbol{r}_{\text{sat}3}}{r^3_{\text{sat}3}}-\frac{\boldsymbol{r}_{\oplus 3}}{r^3_{\oplus 3}}\right). \tag{5}$$

$$\frac{d}{dt}\underbrace{\begin{pmatrix}a\\ e\\ i\\ \omega\\ \Omega\\ \theta\end{pmatrix}}_{\dot{\boldsymbol{x}}}=\underbrace{\begin{pmatrix}\frac{2a^2}{\sqrt{\mu a(1-e^2)}}e\sin(\theta) & \frac{2a^2}{\sqrt{\mu a(1-e^2)}}(1+e\cos(\theta)) & 0\\ \sqrt{\frac{a(1-e^2)}{\mu}}\sin(\theta) & \sqrt{\frac{a(1-e^2)}{\mu}}\frac{2\cos(\theta)+e(1+\cos^2(\theta))}{1+e\cos(\theta)} & 0\\ 0 & 0 & \sqrt{\frac{a(1-e^2)}{\mu}}\frac{\cos(\omega+\theta)}{1+e\cos(\theta)}\\ -\sqrt{\frac{a(1-e^2)}{\mu}}\frac{\cos(\theta)}{e} & \sqrt{\frac{a(1-e^2)}{\mu}}\frac{(2+e\cos(\theta))\sin(\theta)}{e(1+e\cos(\theta))} & -\sqrt{\frac{a(1-e^2)}{\mu}}\frac{\sin(\omega+\theta)}{\tan(i)(1+e\cos(\theta))}\\ 0 & 0 & \sqrt{\frac{a(1-e^2)}{\mu}}\frac{\sin(\omega+\theta)}{\sin(i)(1+e\cos(\theta))}\\ \sqrt{\frac{a(1-e^2)}{\mu}}\frac{\cos(\theta)}{e} & -\sqrt{\frac{a(1-e^2)}{\mu}}\frac{(2+e\cos(\theta))\sin(\theta)}{e(1+e\cos(\theta))} & 0\end{pmatrix}}_{\text{denote as }\mathbf{P}(\mathbf{x})}\begin{pmatrix}f_r\\ f_\theta\\ f_z\end{pmatrix}$$
$$+\underbrace{\begin{pmatrix}0\\0\\0\\0\\0\\ \sqrt{\frac{\mu}{a^3}}\frac{(1+e\cos(\theta))^2}{\sqrt{(1-e^2)^3}}\end{pmatrix}}_{\text{denote as }\mathbf{b}(\mathbf{x})} \tag{8}$$

Here μ_3 is the gravitational parameter of the third-body. $\boldsymbol{r}_{\oplus\text{sat}}$, $\boldsymbol{r}_{\text{sat}3}$ and $\boldsymbol{r}_{\oplus 3}$ are the position vectors from the Earth to satellite, satellite to the third body and Earth to the third body expressed in the Earth Centred inertial (ECI) frame respectively. By expanding the term $\frac{\boldsymbol{r}_{\text{sat}3}}{r^3_{\text{sat}3}}$ in Eq. (5) using Legendre polynomials, we have

$$\ddot{\boldsymbol{r}}_{\oplus\text{sat}}=-\frac{\mu_\oplus\boldsymbol{r}_{\oplus\text{sat}}}{r^3_{\oplus\text{sat}}}$$
$$-\mu_3\left(\frac{-\boldsymbol{r}_{\text{sat}3}(3B+3B^2+B^3)+\boldsymbol{r}_{\oplus\text{sat}}}{r^3_{\oplus 3}}\right), \tag{6}$$

$$B=\sum_{j=1}^{\infty}P_j[\cos\varsigma]\left(\frac{r_{\oplus sat}}{r_{\oplus 3}}\right)^j. \tag{7}$$

Here ς is the angle between $\boldsymbol{r}_{\oplus 3}$ and $\boldsymbol{r}_{\oplus sat}$. Equation (7) can be partitioned as $\mathrm{B}=\mathrm{B}_1+\mathrm{B}_2+\mathrm{B}_3+\cdots$. As in [13], this work utilizes the following dynamic model for the third-body gravitational accelerations. For the Sun, we use the B_1 and B_2 terms. For the Moon, the B_1, B_2 and B_3 terms are considered when $A/m\geq 0.1$ kg/m^2, while the B_4 and B_5 terms are also taken into consideration when $A/m\geq 0.001$ kg/m^2.

2.3 System modelling

This work takes the classical orbital elements $\boldsymbol{x}=[a\;e\;i\;\omega\;\Omega\;\theta]$ as the state. The time derivative of the state is given by [19, page 636]

Here f_r, f_θ, f_z denote the perturbative forces in the local-vertical local-horizontal ($\boldsymbol{LVLH}$, denoted as $\mathcal{F}_o$) frame. μ is the Earth's gravitational parameter.

To express the acceleration due to SRP, a new frame $\mathcal{F}_s$ is constructed. As depicted in Fig. 2a, axis $\boldsymbol{s}_1$ is aligned with Sun-line vector (points from the Sun to satellite) $\boldsymbol{u}$, axis $\boldsymbol{s}_3$

SPI Journal: 42401 MS: 0089 TYPESET DISK LE CP Disp.:2021/6/6 Pages: 12 Layout: Large

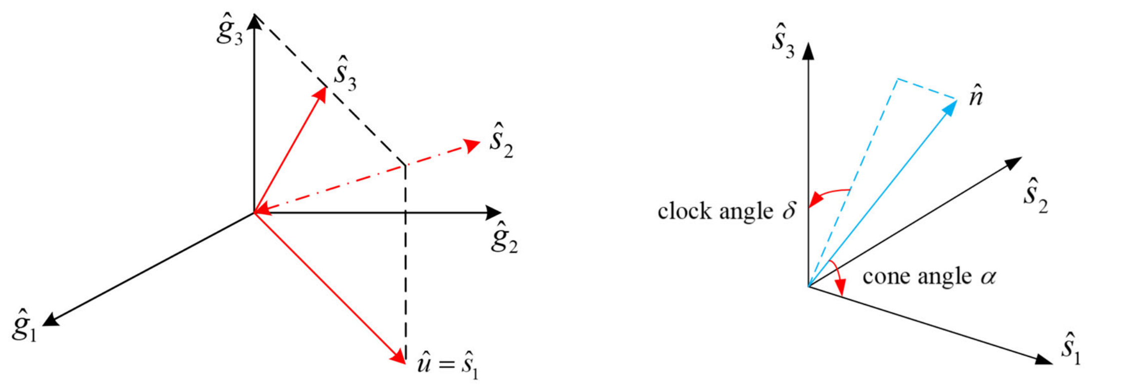

(a) The $\mathcal{F}_s$ Frame (b) Cone Angle and Clock Angle in $\mathcal{F}_s$

Fig. 2 Express SRP in the constructed frame $\mathcal{F}_s$

lies in the plane constructed by $\boldsymbol{s}_1$ and $\boldsymbol{g}_3$ (with $\mathcal{F}_g$ being the ECI frame) and being perpendicular to $\boldsymbol{s}_1$, and axis $\boldsymbol{s}_2$ completes the right hand rule. The rotation matrix from $\mathcal{F}_s$ to $\mathcal{F}_g$ is given by $\boldsymbol{C}_{GS} = \vec{\boldsymbol{f}}_g \cdot \vec{\boldsymbol{f}}_s^T$, in which $\vec{\boldsymbol{f}}_g$ defines the vectrix denoted as $\vec{\boldsymbol{f}}_g = (\boldsymbol{g}_1,\ \boldsymbol{g}_2,\ \boldsymbol{g}_3)^T$ and similarly $\vec{\boldsymbol{f}}_s = (\boldsymbol{s}_1,\ \boldsymbol{s}_2,\ \boldsymbol{s}_3)^T$.

The sail normal vector $\boldsymbol{n}$ in $\mathcal{F}_s$ is given by $\boldsymbol{n} = [\cos\alpha, \sin(\alpha)\sin(\delta), \sin(\alpha)\cos(\delta)]^T$, and the sail transverse vector $\boldsymbol{t} = [\sin\alpha, -\cos(\alpha)\sin(\delta), -\cos(\alpha)\cos(\delta)]^T$ ($\alpha \neq 0$), $\boldsymbol{t} = \boldsymbol{0}$ ($\alpha = 0$), where α and δ are the cone angle and clock angle of the sail (Fig. 2b). For ideal solar sails, the acceleration due to SRP in $\mathcal{F}_s$ can be expressed as $\boldsymbol{f}_{\text{ideal}} = 2P_\odot \cdot (A/m) \cdot \cos^2(\alpha) \cdot \boldsymbol{n}$. For realistic flat solar sails, the acceleration caused by SRP in $\mathcal{F}_s$ is equal to $\boldsymbol{f}_{\text{real}} = \boldsymbol{f}_n + \boldsymbol{f}_t$, where $\boldsymbol{f}_n$ and $\boldsymbol{f}_t$ are the accelerations in the sail normal and sail transverse directions respectively, and are given in Eq. (3). Using Eq. (8), the dynamic system for an ideal solar sail is given by

$$\dot{\boldsymbol{x}}(t) = \boldsymbol{P}(\boldsymbol{x}) \cdot \boldsymbol{C}_{OP}\boldsymbol{C}_{PG}\boldsymbol{C}_{GS} \cdot \boldsymbol{f}_{\text{ideal}} + \boldsymbol{b}(\boldsymbol{x}). \tag{9}$$

For a realistic flat solar sail,

$$\dot{\boldsymbol{x}}(t) = \boldsymbol{P}(\boldsymbol{x}) \cdot \boldsymbol{C}_{OP}\boldsymbol{C}_{PG}\boldsymbol{C}_{GS} \cdot (\boldsymbol{f}_n + \boldsymbol{f}_t) + \boldsymbol{b}(\boldsymbol{x}). \tag{10}$$

Here $\boldsymbol{C}_{OP} = \boldsymbol{C}_3(\theta)$, $\boldsymbol{C}_{PG} = \boldsymbol{C}_3(\omega)\boldsymbol{C}_1(i)\boldsymbol{C}_3(\Omega)$ are rotation matrices from the perifocal coordinate frame (denoted as $\mathcal{F}_p$) to $\mathcal{F}_o$ and from $\mathcal{F}_g$ to $\mathcal{F}_p$ respectively. The SRP accelerations $\boldsymbol{f}_{\text{ideal}}$, $\boldsymbol{f}_n$ and $\boldsymbol{f}_t$ are determined by the sail normal vector $\boldsymbol{n}$ and the sail transverse vector $\boldsymbol{t}$, which are controlled by the control angles α and δ.

Table 4 summarizes the differences between the ideal solar sails and the realistic flat solar sails.

3 Control approach

3.1 Linearization along a nominal trajectory

Consider the dynamic systems in Eqs. (9) and (10) with a disturbance term, $\dot{\boldsymbol{x}}(t) = \boldsymbol{g}(\boldsymbol{x}(t), \boldsymbol{u}(t), \boldsymbol{d}(t))$, where $\boldsymbol{u} = [\alpha,\ \delta]^T$. Linearizing the system along the nominal trajectory $\{\boldsymbol{x}_n(t), \boldsymbol{u}_n(t), \boldsymbol{d}_n(t)\}$ results in

$$\begin{aligned}\dot{(\delta\boldsymbol{x})} = &\underbrace{\frac{\partial \boldsymbol{g}}{\partial \boldsymbol{x}}[\boldsymbol{x}_n, \boldsymbol{u}_n, \boldsymbol{d}_n]}_{\text{denote as } \mathbf{A}(t)}\delta\boldsymbol{x} + \underbrace{\frac{\partial \boldsymbol{g}}{\partial \boldsymbol{u}}[\boldsymbol{x}_n, \boldsymbol{u}_n, \boldsymbol{d}_n]}_{\text{denote as } \mathbf{B}(t)}\delta\boldsymbol{u} \\ &+ \frac{\partial \boldsymbol{g}}{\partial \boldsymbol{d}}[\boldsymbol{x}_n, \boldsymbol{u}_n, \boldsymbol{d}_n]\delta\boldsymbol{d},\end{aligned} \tag{11}$$

where $\delta\boldsymbol{x} = \boldsymbol{x} - \boldsymbol{x}_n$, $\delta\boldsymbol{u} = \boldsymbol{u} - \boldsymbol{u}_n$ and $\delta\boldsymbol{d} = \boldsymbol{d} - \boldsymbol{d}_n$ are deviations from the nominal trajectory, nominal control input and nominal disturbance respectively. Note that $\frac{\partial \boldsymbol{g}}{\partial \boldsymbol{d}}[\boldsymbol{x}_n, \boldsymbol{u}_n, \boldsymbol{d}_n] = 1$, and $\delta\boldsymbol{d} = \boldsymbol{d}_n - \boldsymbol{d}_n = \boldsymbol{0}$. Defining $\boldsymbol{X} \triangleq \delta\boldsymbol{x}$, $\boldsymbol{U} \triangleq \delta\boldsymbol{u}$, Eq. (11) becomes

$$\dot{\boldsymbol{X}}(t) = \boldsymbol{A}(t)\boldsymbol{X}(t) + \boldsymbol{B}(t)\boldsymbol{U}(t). \tag{12}$$

This is a linear time varying (LTV) system, where $\boldsymbol{A}(t)$, $\boldsymbol{B}(t)$ are modelled along the nominal trajectory $\{\boldsymbol{x}_n(t), \boldsymbol{u}_n(t), \boldsymbol{d}_n(t)\}$.

If the state $\boldsymbol{X}(t) = \boldsymbol{x} - \boldsymbol{x}_n(t)$ in the linearized system (Eq. (12)) tracks the desired trajectory $\boldsymbol{Z}(t)$ defined as $\boldsymbol{x}_d(t) - \boldsymbol{x}_n(t)$, then $\boldsymbol{x}(t) = \boldsymbol{x}_d(t)$, which is the desired situation. Therefore, it turns out to be a tracking problem [20, Sec. 9.9]. We seek to minimize the cost functional

$$\begin{aligned}&\mathcal{J}(\boldsymbol{X}(t), \boldsymbol{Z}(t), \boldsymbol{U}(t)) \\ &= \frac{1}{2}\boldsymbol{e}^T(t_f)\boldsymbol{S}\boldsymbol{e}(t_f)\end{aligned}$$

SPI Journal: 42401 MS: 0089 ☐ TYPESET ☐ DISK ☐ LE ☐ CP Disp.:2021/6/6 Pages: 12 Layout: Large

Table 4 Comparisons between the ideal solar sails and the realistic flat solar sails

Solar sail thrust model	
Ideal sail	$\boldsymbol{f}_{\text{ideal}} = \left[2P_{\odot} \cdot (A/m) \cdot \cos^2\alpha\right]\boldsymbol{n}$
Realistic	$\boldsymbol{f}_{\text{real}} = \boldsymbol{f}_n + \boldsymbol{f}_t$
Flat	$\boldsymbol{f}_n = \left(P_{\odot}\frac{A}{m}\left[(1+\tilde{r}s)\cos^2\alpha + B_f(1-s)\tilde{r}\cos\alpha + (1-\tilde{r})\frac{\xi_f B_f - \xi_b B_b}{\xi_f+\xi_b}\cos\alpha\right]\right)\boldsymbol{n}$
Sail	$\boldsymbol{f}_t = \left(P_{\odot}\frac{A}{m}(1-\tilde{r}s)\cos\alpha\sin\alpha\right)\boldsymbol{t}$
Control angle constraints	
Ideal sail	$\alpha \in [0°, 90°]$, $\delta \in [0°, 360°]$
Realistic flat sail	$\alpha \in [0°, 85°]$, $\delta \in [0°, 360°]$
System dynamics	
Ideal sail	$\dot{\boldsymbol{x}}(t) = \boldsymbol{P}(\boldsymbol{x}) \cdot \boldsymbol{C}_{OP}\boldsymbol{C}_{PG}\boldsymbol{C}_{GS} \cdot \boldsymbol{f}_{\text{ideal}} + \boldsymbol{b}(\boldsymbol{x})$
Realistic flat sail	$\dot{\boldsymbol{x}}(t) = \boldsymbol{P}(\boldsymbol{x}) \cdot \boldsymbol{C}_{OP}\boldsymbol{C}_{PG}\boldsymbol{C}_{GS} \cdot (\boldsymbol{f}_n + \boldsymbol{f}_t) + \boldsymbol{b}(\boldsymbol{x})$

$$+\int_{t_0}^{t_f}\left(\frac{1}{2}\boldsymbol{e}^T(t)\boldsymbol{Q}\boldsymbol{e}(t) + \frac{1}{2}\boldsymbol{U}^T(t)\boldsymbol{R}\boldsymbol{U}(t)\right)\mathrm{d}t, \tag{13}$$

where $\boldsymbol{e}(t) = \boldsymbol{X}(t) - \boldsymbol{Z}(t)$ denotes the tracking error. The matrix $\boldsymbol{S} = \boldsymbol{S}^T \geq 0$ penalizes the terminal tracking error, $\boldsymbol{Q} = \boldsymbol{Q}^T \geq 0$ penalizes the tracking error, and $\boldsymbol{R} = \boldsymbol{R}^T > 0$ penalizes the control inputs. The solution of this problem can be obtained from Eq. (51) in [13] by setting the disturbance term to zero, and is given by:

$$\boldsymbol{U}^*(t) = -\boldsymbol{R}^{-1}\boldsymbol{B}^T(t)\left(\boldsymbol{G}(t)\boldsymbol{X}(t) - \boldsymbol{g}(t)\right), \tag{14}$$

where $\boldsymbol{G}(t)$ and $\boldsymbol{g}(t)$ can be calculated by integrating the following equations simultaneously backward:

$$\dot{\boldsymbol{G}}(t) = -\boldsymbol{Q} - \boldsymbol{A}^T(t)\boldsymbol{G}(t) - \boldsymbol{G}(t)\boldsymbol{A}(t) + \boldsymbol{G}(t)\boldsymbol{B}(t)\boldsymbol{R}^{-1}\boldsymbol{B}^T(t)\boldsymbol{G}(t), \tag{15}$$

$$\dot{\boldsymbol{g}}(t) = -\boldsymbol{Q}\boldsymbol{Z}(t) - \left(\boldsymbol{A}^T(t) - \boldsymbol{G}(t)\boldsymbol{B}(t)\boldsymbol{R}^{-1}\boldsymbol{B}^T(t)\right)\boldsymbol{g}(t), \tag{16}$$

using the boundary conditions

$$\boldsymbol{G}(t_f) = \boldsymbol{S}, \tag{17}$$

$$\boldsymbol{g}(t_f) = \boldsymbol{S}\boldsymbol{Z}(t_f). \tag{18}$$

3.2 Iterations of linearization

Since the linearization in Sect. 3.1 is along a nominal trajectory, the linearized system is not completely accurate, and this causes the terminal state error between the terminal state and the desired state. In this work, we apply the "iterations of linearization" control approach to gradually reduce the inaccuracy of the linearized systems, as well as the terminal state error.

As described in Fig. 3, the dynamic system is first linearized along a nominal trajectory, then the linear feedback controller described in Setc. 3.1 is applied to reduce the terminal state error based on the linearized system. The resultant actual trajectory acts as a nominal trajectory for the linearization in the next iteration. The iterations are applied until the terminal state error is smaller then the error threshold.

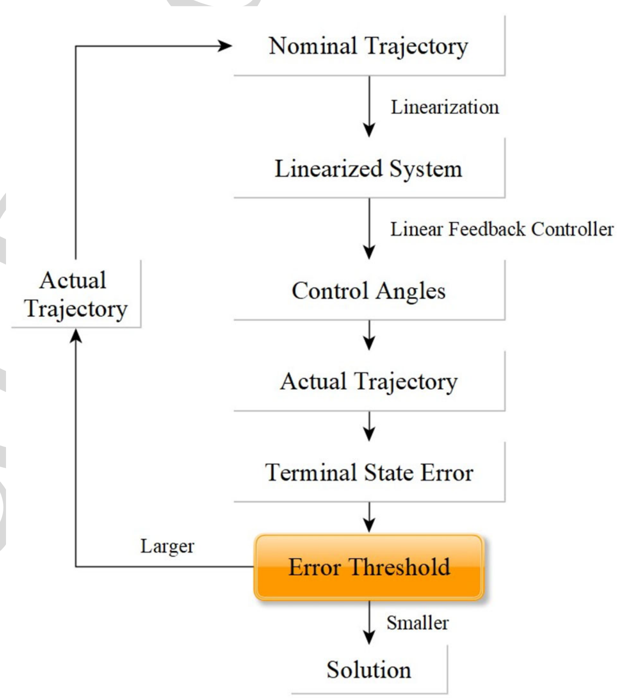

Fig. 3 The iterations of linearization

In theory, the applied "iterations of linearization" control approach is only able to find a quasi-local optimal solution. A quasi-local optimal solution is acceptable for the end-of-life GEO satellites removal mission, since the GEO graveyard region is broad and the requirements on the orbital elements are not strict. The applied "iterations of linearization" control approach significantly reduces the terminal state error in

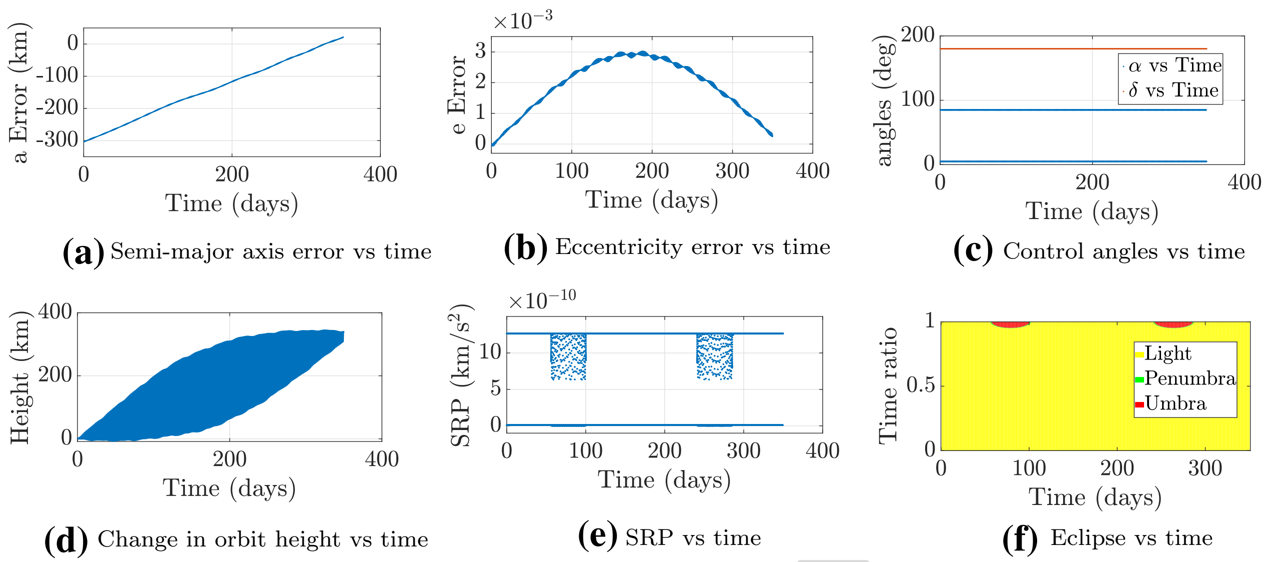

(a) Semi-major axis error vs time **(b)** Eccentricity error vs time **(c)** Control angles vs time

(d) Change in orbit height vs time **(e)** SRP vs time **(f)** Eclipse vs time

Fig. 4 Nominal trajectory for the ideal solar sail

[13], as well as the computation cost caused by the numerical approach proposed in [14].

4 End-of-life GEO satellites removal

The control objective is to raise the orbit semi-major axis by 305 km and make the eccentricity of the final orbit smaller than 10^{-4}. In this way, the perigee of the final orbit will be raised slightly more than 300 km, thus the final orbit will be placed in the GEO graveyard region. The desired semi-major axis $a_d = 42164$ km + 305 km = 42469 km, and the desired eccentricity $e_d = 10^{-4}$. To avoid the singularity of the classical orbital elements, the desired eccentricity of the final orbit is set to be a small but non-zero number (10^{-4}).

The initial position of the satellite in the ECI frame is set to be [0.0 m, 42164.8 km, 1.0 m]. The initial time is Jan 1st, 2017, 00 : 00 : 00, with the time constants ΔUT (UT1 − UTC) = 0.359485 s, ΔAT(TAI − UTC) = 37.0 s. The final time t_f = 350 days. The orbit is propagated using the 4th-order Runge–Kutta (RK4) formula, and the time step is set to be 30 s. Compared to the simulation time length (350 days), setting a time step of 30 s is appropriate to preserve numerical accuracy, and in the meantime causes an acceptable computation cost.

4.1 Removal using ideal solar sails

The A/m of spacecraft is set to be 0.14 kg/m^2. Figure 4 presents the nominal trajectory for the first linearization. In the nominal trajectory, the cone angle α is 5° when the satellite is moving away from the Sun, and 85° when moving toward. Each of the 5° and 85° period lasts about half an orbit (12 h for a GEO satellite). The clock angle δ is equal to 180° all the time. In Fig. 4a, b, the terminal state error for the semi-major axis and eccentricity is +22.6427 km and $+2.3376 \times 10^{-4}$ respectively. The change of the orbit height, SRP magnitude and eclipse time ratio are shown in Fig. 4d–f respectively.

Figure 5 presents the actual trajectory after the first linearization. The penalty matrices in Eq. (13) are set to be $\boldsymbol{S} = \text{diag}[10^3,\ 10^{12},\ 1,\ 1,\ 1,\ 1]$, $\boldsymbol{Q} = \text{diag}[10,\ 10^9,\ 1,\ 1,\ 1,\ 1]$, $\boldsymbol{R} = \text{diag}[10^{16},\ 10^{16}]$. Figure 5a–d present the feedback and total control angles. In Fig. 5e, f, the terminal state error of the semi-major axis and eccentricity is +18.1682 km and $+1.0856 \times 10^{-4}$ respectively.

The terminal state error in Fig. 5 originates from the inaccuracy of the linearized system. Since the linearization is along a nominal trajectory, the linearized system is not completely accurate. To gradually reduce the inaccuracy of the linearized systems, we apply the "iterations of linearization" control approach. We linearize the system along the actual trajectory generated by the previous step of linearization, and apply the same linear feedback controller to further reduce the terminal state error. The iterations of linearization are applied until the terminal state error is smaller than the cost threshold.

Table 5 presents the history of the terminal state error in each step of linearization. The terminal state error decreases in each step of linearization, and a solution (presented in Fig. 6) is generated after the fourth linearization. The terminal state error of the semi-major axis and eccentricity is +0.7142 km and -3.5862×10^{-5} respectively. From Table 5 we also see that, although the terminal state error in this

SPI Journal: 42401 MS: 0089 TYPESET DISK LE CP Disp.:2021/6/6 Pages: 12 Layout: Large

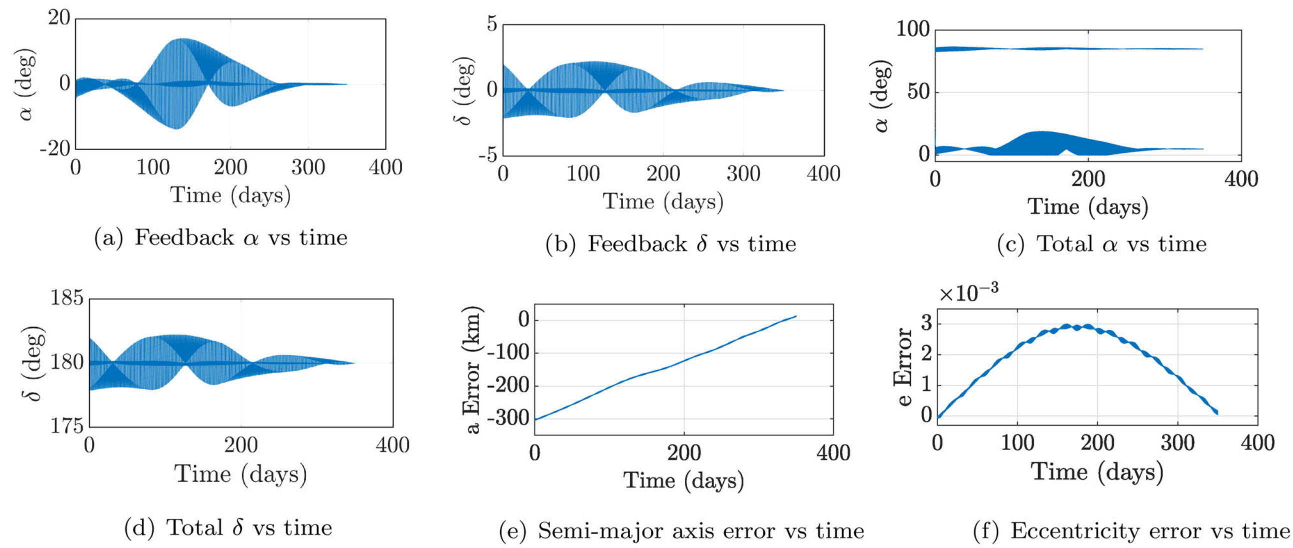

Fig. 5 Real-time trajectory for the ideal solar sail, first linearization

Table 5 History of the ideal solar sail optimization

	Terminal a error (km)	Terminal e error	Cost value	CPU time (min)
Nominal trajectory	+22.6427	$+2.3376\times10^{-4}$	$+2.56\times10^{8}$	29
1st Linearization	+18.1682	$+1.0856\times10^{-4}$	$+1.26\times10^{8}$	104
2nd Linearization	+14.1226	$+0.9013\times10^{-4}$	$+1.04\times10^{8}$	
3rd Linearization	+3.1774	$+7.5862\times10^{-5}$	$+7.90\times10^{7}$	
4th Linearization	+0.7142	-3.5862×10^{-5}	$+3.65\times10^{7}$	
Ref. [14]	+0.0903	-4.0962×10^{-6}	$+4.19\times10^{6}$	18098

The desired semi-major axis $a_d = 42469$ km, the desired eccentricity $e_d = 10^{-4}$. (Using an Intel i5-9600K CPU @ 3.70GHz, 48.0 GB RAM Laptop for Calculation)

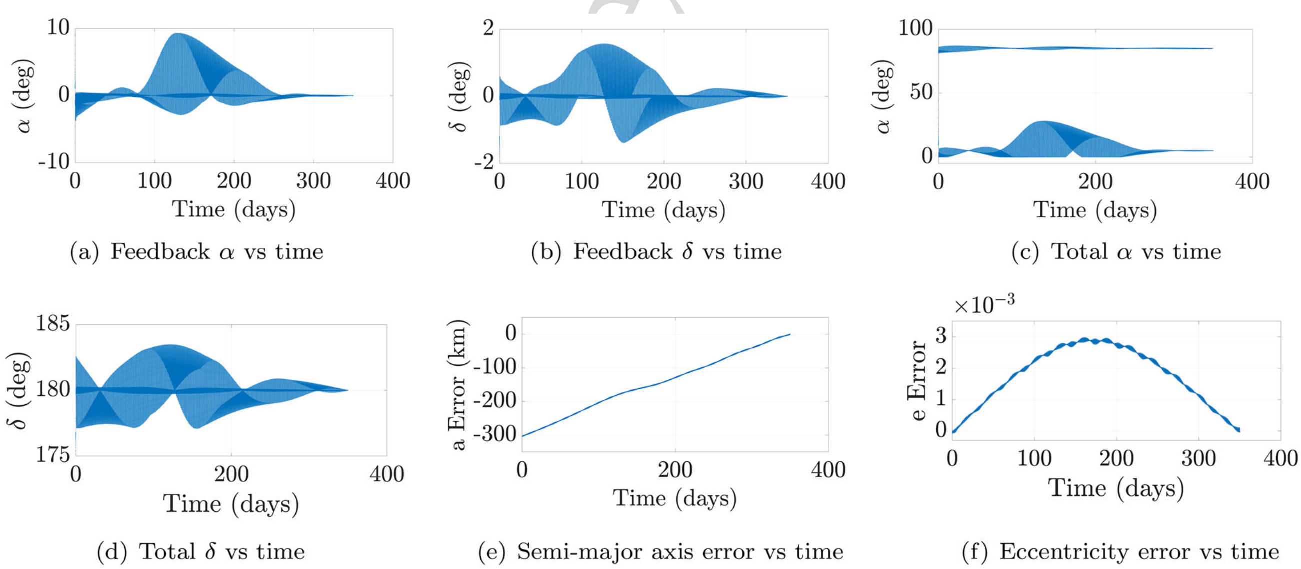

Fig. 6 Real-time trajectory for the ideal solar sail, fourth linearization

SPI Journal: 42401 MS: 0089 TYPESET DISK LE CP Disp.:2021/6/6 Pages: 12 Layout: Large

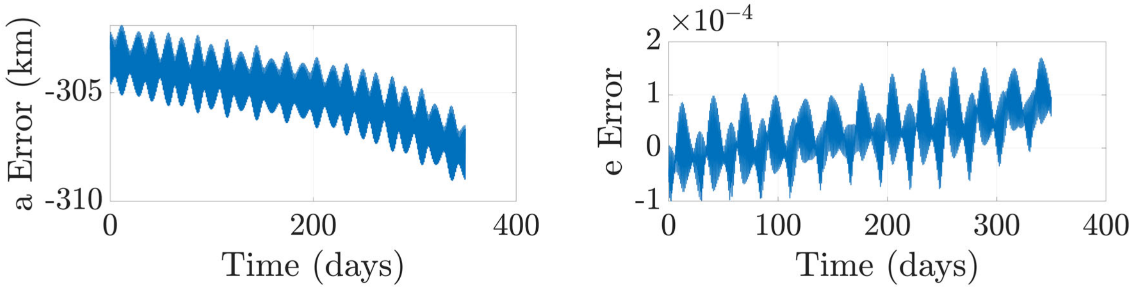

(a) Semi-major axis error vs time (b) Eccentricity error vs time

Fig. 7 Influence of the Leeward force on the orbital elements

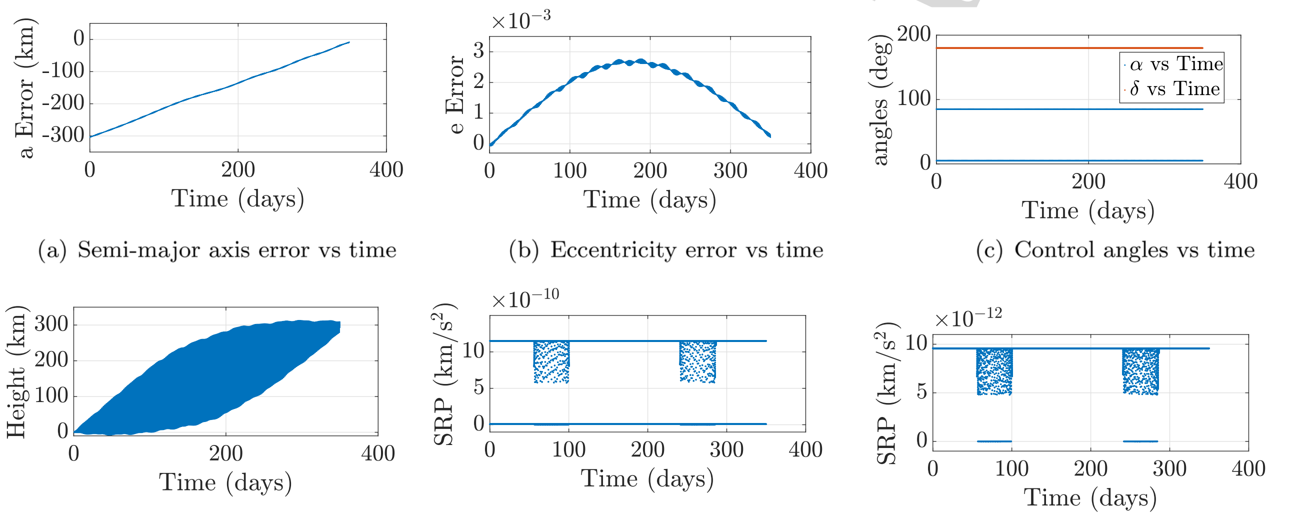

(a) Semi-major axis error vs time (b) Eccentricity error vs time (c) Control angles vs time

(d) Change in orbit height vs time (e) SRP in the sail normal direction vs time (f) SRP in the sail transverse direction vs time

Fig. 8 Nominal trajectory for the realistic flat solar sail, $A/m = 0.14\ \mathrm{kg/m^2}$

work is slightly larger than in [14], the computation time is significantly reduced from 18098 to 104 min.

4.2 Removal using realistic flat solar sails

As described in Sect. 2, the constraint in the sail cone angle results in a so-called "leeward force", which always exits along the Sun-sail direction and will decrease the orbit altitude when the satellites move toward the Sun. Figure 7 shows the influence of the "leeward force" on the orbital elements in the satellite removal mission. We can see that there is a reduction about 8 km in the semi-major axis, and an increase about 1.8×10^{-4} in the orbit eccentricity. Figure 8 presents the nominal trajectory of the realistic flat sail with a spacecraft A/m of $0.14\ \mathrm{kg/m^2}$. In Fig. 8, the terminal semi-major axis and eccentricity error is -9.1092 km and $+2.1683 \times 10^{-4}$ respectively.

We gradually increase the A/m of spacecraft and adjust the nominal control angles to find a nominal trajectory in which the terminal semi-major axis and eccentricity are close to the desired ones. After some trial and error, the resultant nominal trajectory is presented in Fig. 9. In the nominal trajectory, the A/m of spacecraft is equal to $0.16\ \mathrm{kg/m^2}$. The cone angle α is 13° when the satellite is moving away from the Sun, and 77° when moving toward. Each of the 13° and 77° period lasts about half an orbit (12 h for a GEO satellite). The clock angle δ is equal to 180° all the time. In Fig. 9a, b, the terminal state error for the semi-major axis and eccentricity is + 3.8710 km and $+8.1504 \times 10^{-5}$ respectively. The change in orbit height and the magnitude of SRP in the sail normal/transverse direction are shown in Fig. 9d–f respectively. From Fig. 9 (d)(e) we see that, the magnitude of SRP in the sail transverse direction is 2 magnitudes smaller than that in the sail normal direction. However, since the removal time is very long (350 days), the tiny "leeward force" resulting from sail cone angle constraint still has evident negative impact on the removal mission. From the nominal trajectory

SPI Journal: 42401 MS: 0089 TYPESET DISK LE CP Disp.:2021/6/6 Pages: 12 Layout: Large

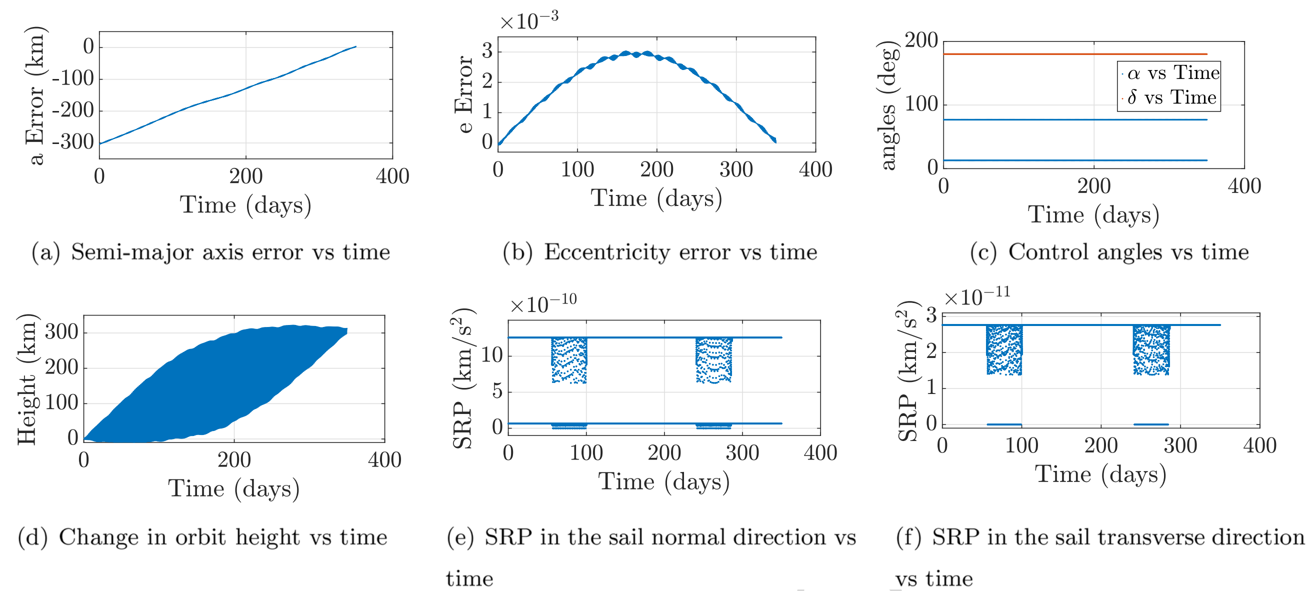

(a) Semi-major axis error vs time (b) Eccentricity error vs time (c) Control angles vs time

(d) Change in orbit height vs time (e) SRP in the sail normal direction vs time (f) SRP in the sail transverse direction vs time

Fig. 9 Nominal trajectory for the realistic flat solar sail, $A/m = 0.16$ kg/m^2

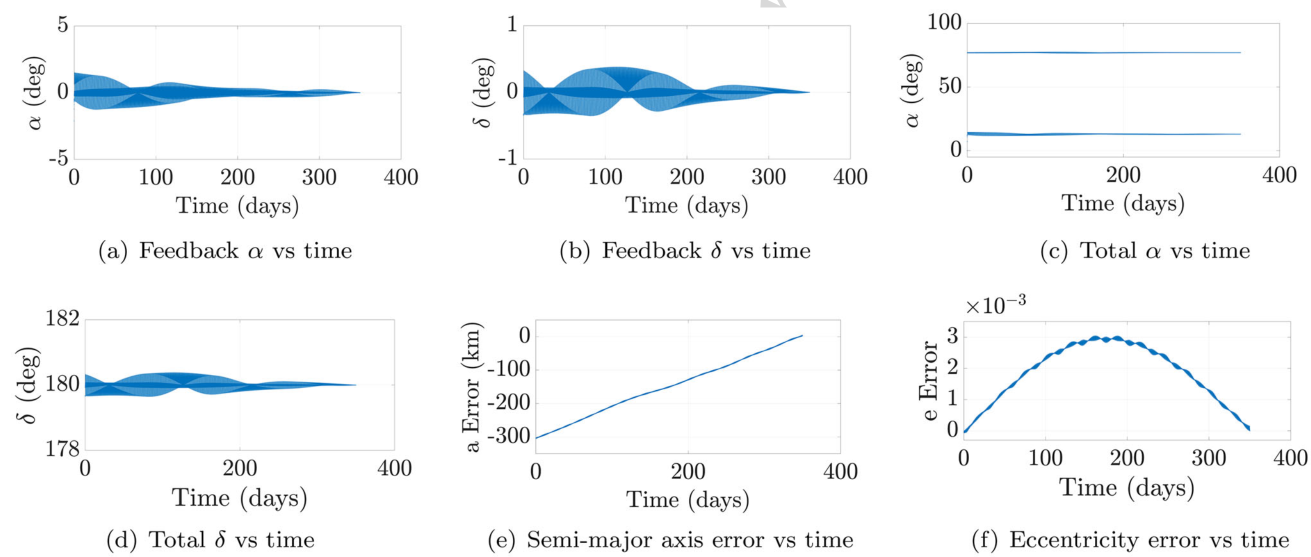

(a) Feedback α vs time (b) Feedback δ vs time (c) Total α vs time

(d) Total δ vs time (e) Semi-major axis error vs time (f) Eccentricity error vs time

Fig. 10 Real-time trajectory for the realistic flat solar sail, first linearization

in Fig. 9 we can find that, this negative impact causes an increase in the A/m of spacecraft from 0.14 to 0.16 kg/m^2.

Figure 10 presents the actual trajectory after the first linearization. The penalty matrices in Eq. (13) are set to be $\boldsymbol{S} = \mathrm{diag}[10^3,\ 10^{12},\ 1,\ 1,\ 1,\ 1]$, $\boldsymbol{Q} = \mathrm{diag}[10,\ 10^9,\ 1,\ 1,\ 1,\ 1]$, $\boldsymbol{R} = \mathrm{diag}[10^{16},\ 10^{16}]$. Figure 10a–d present the feedback and total control angles. From Fig. 10a, b we see that the feedback control angles gradually approach zero. Figure 10c, d present the total control angles. In Fig. 10e, f, the terminal state error of the semi-major axis and eccentricity is +3.1877 km and $+3.9237 \times 10^{-5}$ respectively.

Table 6 presents the history of the terminal state error in each step of linearization. The value of the cost function decreases in each step of linearization, and a solution (presented in Fig. 11) is generated after the third linearization. The terminal state error of the semi-major axis and eccentricity is +4.3479 and -5.1340×10^{-6} respectively.

From Tables 5 and 6 we can find that, the negative impact of using realistic flat solar sails in the end-of-life GEO satellite removal mission is evident but not significant. To achieve end-of-life GEO satellites removal to the GEO graveyard region using realistic flat solar sails in 350 days, a small increase in the A/m of spacecraft from 0.14 to 0.16 kg/m^2 is required.

Table 6 History of the realistic flat solar sail optimization

	Terminal a error (km)	Terminal e error	Cost value	CPU time (min)
Nominal trajectory	+3.8710	$+8.1504\times10^{-5}$	$+8.54\times10^{7}$	30
1st Linearization	+3.1877	$+3.9237\times10^{-5}$	$+4.24\times10^{7}$	78
2nd Linearization	+2.2299	-2.1901×10^{-5}	$+2.41\times10^{7}$	
3rd Linearization	+4.3479	-5.1340×10^{-6}	$+9.48\times10^{6}$	

The desired semi-major axis $a_d = 42469$ km, the desired eccentricity $e_d = 10^{-4}$. (Using an Intel i5-9600K CPU @ 3.70GHz, 48.0 GB RAM Laptop for Calculation)

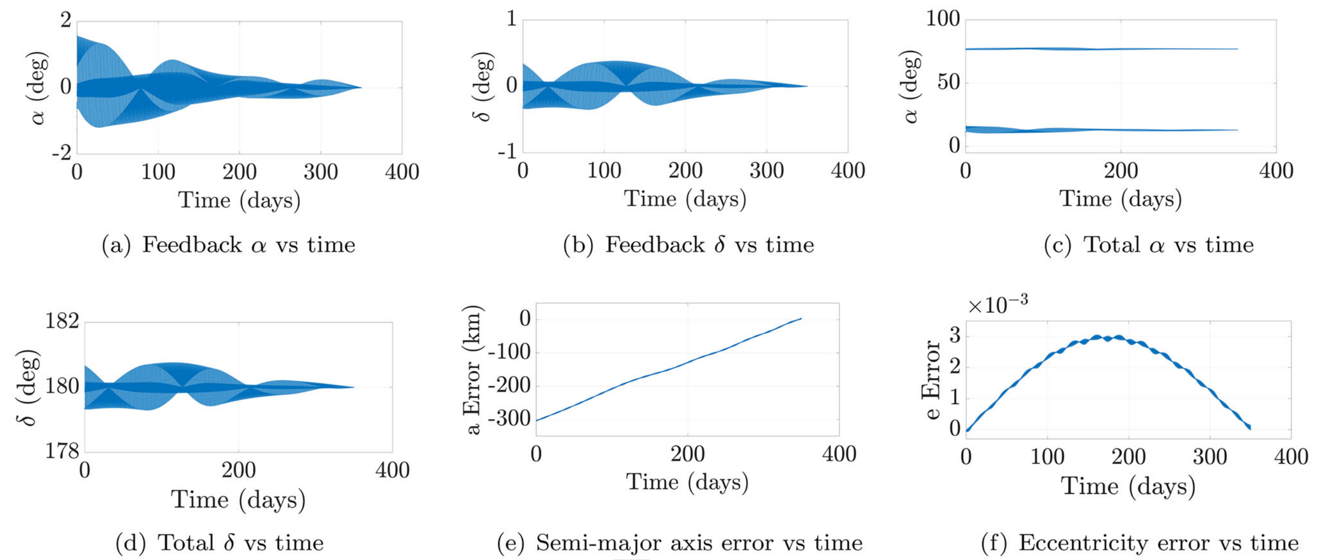

Fig. 11 Real-time trajectory for the realistic flat solar sail, third linearization

5 Conclusions

This paper proposes an analytical solution of removing end-of-life GEO satellites to the GEO graveyard region using realistic flat solar sails. The sail control angles are generated using the linear optimal tracking controller. Iterations of linearization are applied to gradually reduce the inaccuracy of the linearized systems, thus reducing the terminal state error. Simulations indicate that, the negative impact of using realistic flat solar sails in the end-of-life GEO satellite removal mission is evident but not significant. Compared to using ideal solar sails, a small increase in the A/m of spacecraft from 0.14 to 0.16 $\mathrm{kg/m^2}$ is required to achieve the end-of-life GEO satellite removal using realistic flat solar sails in 350 days.

Funding This work was supported by the China Scholarship Council (CSC).

References

1. Anselmo L, Pardini C (2008) Space debris mitigation in geosynchronous orbit. Adv Space Res 41(7):1091–1099. https://doi.org/10.1016/j.asr.2006.12.018
2. Johnson NL (2012) A new look at the geo and near-geo regimes: operations, disposals, and debris. Acta Astronaut 80:82–88. https://doi.org/10.1016/j.actaastro.2012.05.024
3. Anderson PV, Schaub H (2014) Local debris congestion in the geosynchronous environment with population augmentation. Acta Astronaut 94(2):619–628. https://doi.org/10.1016/j.actaastro.2013.08.023
4. ESA (2019) ESAS annual space environment report. issue 3, revision 2. July 2019. ESA. https://www.sdo.esoc.esa.int/environment_report/Space_Environment_Report_latest.pdf
5. ESA (2018) Classification of geosynchronous objects. issue 20, revision 0. May 2018. ESA. http://www.astronomer.ru/data/0128/Classification_of_Geosynchronous_Objects_I20R0.pdf
6. Allen J (2010) The galaxy 15 anomaly: Another satellite in the wrong place at a critical time. Space Weather. https://doi.org/10.1029/2010sw000588
7. IADC (2007) Inter-agency space debris coordination committee. Space debris mitigation guidelines, revision 1, Sep 2007. IADC. http://www.unoosa.org/documents/pdf/spacelaw/sd/IADC-2002-01-IADC-Space_Debris-Guidelines-Revision1.pdf
8. Chao C (1998) Geosynchronous disposal orbit stability. In: AIAA/AAS Astrodynamics Specialist Conference and Exhibit. https://doi.org/10.2514/6.1998-4186
9. Gopinath N, Ganeshan A (2005) Long term evolution of objects in gso-disposal orbit. In: 4th European Conference on Space Debris, vol 587. https://doi.org/10.1007/978-94-009-2285-3_27
10. Borja JA, Tun D (2006) Deorbit process using solar radiation force. J Spacecr Rockets 43(3):685–687. https://doi.org/10.2514/1.9508

11. Kelly PW, Bevilacqua R, Mazal L, Erwin RS (2018) Tugsat: Removing space debris from geostationary orbits using solar sails. J Spacecr Rockets 55(2):437–450. https://doi.org/10.2514/1.a33872
12. Kelly P, Bevilacqua R (2019) An optimized analytical solution for geostationary debris removal using solar sails. Acta Astronaut 162:72–86. https://doi.org/10.1016/j.actaastro.2019.05.055
13. Mei H, Damaren CJ, Zhan X (2020) Hybrid removal of end-of-life geosynchronous satellites using solar radiation pressure and impulsive thrusts. Adv Space Res. https://doi.org/10.1016/j.asr.2020.04.052
14. Mei H, Damaren CJ, Zhan X (2020) Feedback pseudospectral method for end-of-life geostationary satellite removal using solar sailing. J Guid Control Dyn
15. Spencer H, Carroll KA (2014) Real solar sails are not ideal, and yes it matters. In: Advances in solar sailing. Springer, New York, pp 921–940. https://doi.org/10.1007/978-3-642-34907-2_55
16. Simo J, McInnes CR (2016) Potential effects of a realistic solar sail and comparison to an ideal sail. In: 26th AAS/AIAA Space flight mechanics meeting, Napa, CA, USA, 14-18 Feb 2016, pp. 3106–3120. https://eprints.gla.ac.uk/129011/1/129011.pdf
17. Campbell BA, Thomas SJ (2014) Realistic solar sail thrust. In: Advances in solar sailing. Springer, New York, pp 407–435. https://doi.org/10.1007/978-3-642-34907-2_27
18. McInnes CR (2004) Solar sailing: technology, dynamics and mission applications. Springer, New York
19. Vallado DA (2001) Fundamentals of astrodynamics and applications, vol 12. Springer, New York
20. Athans M, Falb PL (2013) Optimal control: an introduction to the theory and its applications. Courier Corporation, Chelmsford

SPI Journal: **42401** MS: **0089** TYPESET DISK LE CP Disp.:**2021/6/6** Pages: **12** Layout: **Large**